Accurate Induction Machines Efficiency Mapping Computed by Standard Test Parameters

Accurate Induction Machines Efficiency Mapping Computed by Standard Test Parameters

Ornella Stiscia, *Student Member, IEEE*, Sandro Rubino, *Member, IEEE*, Silvio Vaschetto, *Senior Member, IEEE*, Andrea Cavagnino, *Fellow, IEEE,* and Alberto Tenconi, *Senior Member, IEEE*

***Abstract*— The extensive electrification process that is taking hold in several applications makes increasingly necessary the virtualization of electric components for energetic and performance assessments during the system design stage. For this purpose, this paper proposes a straightforward methodology for computing the efficiency maps of induction machines operated in wide torque-speed ranges. The modeling approach is based on the induction machine equivalent circuit defined in the rotor *dq* coordinates. The procedure allows computing a set of efficiency maps at different machine temperatures and supply voltage levels, both for motor and generator operation modes. The equivalent circuit parameters at different frequencies and voltages are determined by means of the well-known no-load and locked-rotor tests, thus including in the modelling the machine nonlinearities, skin effect and the iron losses. The proposed methodology has been validated on a 10 kW, 4-pole induction machine. The comparison between computed and experimental efficiency maps for different operating conditions, confirm the validity of the proposed methodology.**

***Index Terms*—efficiency maps, induction machines, standard test procedures, testing, transport electrification, virtualization.**

I. Introduction

In the energy transition pathway towards more efficient and carbon-free solutions, the electrification of a wide range of applications represents a sustainable way to achieve these goals [1]. Such a paradigm shift involves a substantial redesign of several already engineered systems, and their accurate energetic assessment is of primary importance [2]–[4]. From an engineering standpoint, components virtualization is a sustainable approach to perform comprehensive simulations of complex systems, also considering variable load profiles [5]. This allows markedly reducing the need for expensive and time-consuming testing activities.

Manuscript received XXX XX, 2021; revised XXX XX, 2021 and XXXX XX,2021; accepted XXXX XX, 2021. Date of publication XXX XX, 2021; date of current version XXX XX, 202X. Paper 202X-EMC-XXX.RX, presented at the 2020 IEEE Energy Conversion Congress and Exposition, Online Edition, Oct. 11–Oct. 15, and approved for publication in the IEEE TRANSACTIONS ON INDUSTRY APPLICATIONS by the Electric Machines Committee of the IEEE Industry Application Society. (Corresponding author: Ornella Stiscia.).

The authors are with the Politecnico di Torino, Dipartimento Energia "G. Ferraris", Torino, 10129, Italy (e-mail: ornella.stiscia@polito.it, sandro.rubino@polito.it silvio.vaschetto@polito.it; andrea.cavagnino@ polito.it, alberto.tenconi@polito.it).

Color versions of one or more of the figures in this article are available online at https://ieeexplore.ieee.org.Digital Object Identifier XXXXXX.

Focusing on electrical machines, different virtualization alternatives can be considered depending on the required outputs and modeling constraints, such as simulation time and accuracy [6]. For energetic evaluations, models based on machine losses and efficiency usually represent the most convenient solution [7]–[10]. Moreover, different complexity levels can be considered for the energetic model depending on the machine load profile. For instance, a constant efficiency value can conveniently represent the energetic behavior of components operated at fixed working point. On the other hand, for variable operations in wide torque-speed ranges an approach based on efficiency maps is usually adopted [10], [11]. The solutions proposed in literature for computing efficiency maps of electric machines often rely on finite element analyses (FEA) [7], [11]-[20]. Although FEA simulations allow predicting efficiency values avoiding measurements on the real component, thus saving cost for expensive test rigs, details on the machine design data and materials characteristics must be known for the model setup [21]. The literature reports only few contributions that focus on the efficiency mapping of induction machines (IMs) through FEA simulations, and manufacturers usually provide efficiency information only for few working points. Rarely, they provide efficiency maps that refer to a specific machine temperature and a defined supply voltage. Although this level of information may be sufficient for machines operated at a fixed working point, it may not be accurate enough when different working conditions in wide torque-speed ranges are considered. Indeed, in these cases, the supply voltage and the machine temperature can assume very different values depending on the required torque and speed.

If in one hand the efficiency map problem is substantially solved for synchronous PM and IPM machines, on the other hand it still has not been completely addressed for IMs through straightforward approaches. Therefore, this paper aims at computing accurate efficiency maps of IMs operated in wide torque-speed ranges, proposing an effective solution to avoid demanding FEA analyses and expensive experimental mapping procedures. In detail, the proposed approach is based on the IM equivalent circuit which parameters can be easily obtained by the conventional no-load and locked-rotor tests executed at the different voltages and frequencies of interest [22], [23]. The set of measured machine parameters allow modeling the effects of the magnetic saturation, skin effect and iron losses for all the working points in the torque-speed plane. Therefore, multiple

efficiency maps are obtained solving the equivalent circuit in steady-state conditions, considering the temperature impacts on the stator and rotor resistances.

The developed efficiency mapping procedure also considers the supply voltage and current limits on the maximum torque-per-speed profiles achievable by the machine under analysis.

The proposed methodology has been originally presented in [24] and preliminarily validated on an industrial totally enclosed fan-cooled IM supplied by a sinusoidal power source. This paper brings in added value by reporting the step-by-step procedure for performing the efficiency mapping and reports the experimental validation for a 10 kW, 4-pole IM machine supplied by a PWM power converter. The paper also discusses the laboratory setup and data post-elaborations used for the comparison between the efficiency maps measured on the inverter-fed IM and those computed by the proposed mapping approach.

II. Machine Modeling

The proposed efficiency mapping procedure uses the electromagnetic model of the IM defined in the rotating *dq* reference frame, where the *d*-axis is assumed coincident with the position of the rotor flux linkage vector [25]. The steady-state equivalent circuit of the IM using the *dq* components is shown in Fig. 1, and the related voltage equations are listed in (1).

$$\begin{cases} V_{s,d} = R_s \cdot I_{s,d} + E_{s,d} \\ V_{s,q} = R_s \cdot I_{s,q} + E_{s,q} \end{cases}, \quad \begin{cases} E_{s,d} = -\omega_s \cdot \Lambda_{s,q} \\ E_{s,q} = \omega_s \cdot \Lambda_{s,d} \end{cases} \tag{1}$$

The parameter R_s is the stator resistance, R_{Fe} is the equivalent resistance for the iron losses, while the *dq* components of voltage, back-emf, current, and flux linkage stator vectors are denoted with ($V_{s,d}$, $V_{s,q}$), ($E_{s,d}$, $E_{s,q}$), ($I_{s,d}$, $I_{s,q}$), and ($\Lambda_{s,d}$, $\Lambda_{s,q}$), respectively. The synchronous speed is denoted with ω_s.

The magnetic model, that consists of the current-to-flux relationships, is computed as in (2), where L_s is the total stator inductance and σ is the overall leakage factor [26].

$$\begin{cases} \Lambda_{s,d} = L_s \cdot I_{eq,d} \\ \Lambda_{s,q} = \sigma \cdot L_s \cdot I_{eq,q} \end{cases} \tag{2}$$

The *dq* components of flux– and torque–producing currents ($I_{eq,d}$, $I_{eq,q}$) differ from the stator absorbed *dq* currents by the corresponding iron losses current components ($I_{Fe,d}$, $I_{Fe,q}$).

The rotor current components ($I_{r,d}$, $I_{r,q}$) and the flux linkage Λ_r in steady-state conditions can be computed as in (3), where L_m and L_r are the magnetizing and the total rotor inductance, respectively [25], [26].

$$\begin{cases} I_{r,d} = 0 \\ I_{r,q} = -\left(L_m / L_r\right) \cdot I_{eq,q} \end{cases}, \quad \Lambda_r = L_m \cdot I_{eq,d} \tag{3}$$

The electromagnetic torque T_{em} is calculated by (4), where p is the pole pairs number.

$$T_{em} = \frac{3}{2} \cdot p \cdot \left(\Lambda_{s,d} \cdot I_{eq,q} - \Lambda_{s,q} \cdot I_{eq,d}\right) \tag{4}$$

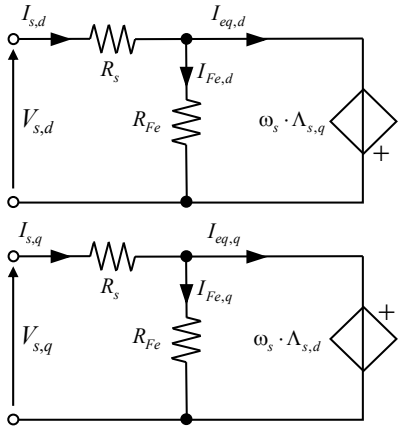

Fig. 1. IM steady-state equivalent circuit in the rotating *dq* reference frame.

Finally, the rotational speed ω_m is computed according to the slip speed ω_{sl} using (5), where R_r is the rotor resistance.

$$\omega_m = \frac{1}{p} \cdot \left(\omega_s - \omega_{sl}\right) \quad , \quad \omega_{sl} = \frac{R_r}{L_r} \cdot \frac{I_{eq,q}}{I_{eq,d}} \tag{5}$$

Although the IM electromagnetic model in (1)–(5) presents simple equations in steady-state conditions, the following nonlinearities need to be considered for accurately computing the IM efficiency maps:

1) the stator resistance R_s depends on the average temperature of the stator winding θ_s, as well as on the frequency of the stator currents f_s, due to the skin effect;
2) the magnetizing inductance L_m is affected by magnetic saturation, whose extent depends on the amplitude of the magnetizing current I_m as:

$$L_m = f\left(I_m\right) \ , \ I_m = \sqrt{{I_{eq,d}}^2 + \left(I_{eq,q} + I_{r,q}\right)^2} \tag{6}$$

3) the iron losses depend on the frequency of the stator currents f_s and the flux density values in the stator lamination or, in other words, by the stator back-electromotive force (back-emf);
4) the rotor resistance R_r depends on the average temperature of the rotor cage θ_r, as well as on the slip frequency f_{sl} because of the significant impact of skin effect in bar conductors in squirrel caged rotors [27];
5) the IM mechanical torque T_m differs from the electromagnetic one (4) by the torque T_{fv} necessary to sustain the friction and ventilation losses:

$$T_m = T_{em} - T_{fv} \tag{7}$$

Along with the above-mentioned nonlinearities, potential saturation effects of the total inductances should also be considered because of their impact on the IM inductances, as expressed in (8).

$$L_s = L_m + L_{ls} \quad , \quad L_r = L_m + L_{lr} \tag{8}$$

In (8) L_{ls} and L_{lr} are the stator and rotor leakage inductances, respectively. These parameters are assumed not saturable and not influenced by the skin effect phenomena.

TABLE I
MACHINE NAMEPLATE DATA

Pole pairs	2
Rated power	10 kW
Rated speed	3000 rpm
Rated torque	16 Nm
Rated voltage	400 V_{rms}
Rated current	10 A_{rms}

TABLE II
MEASURED PARAMETERS

Stator resistance $R_{s,0}$ (θ_0 = 25°C)	634 mΩ
Locked-rotor inductance L_{cc}	7.63 mH
Stator leakage inductance L_{ls}	3.815 mH
Rotor leakage inductance L_{lr}	3.815 mH

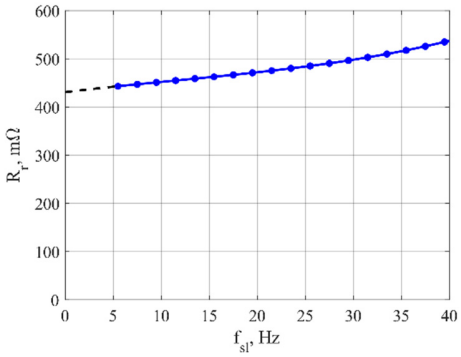

Fig. 2. Rotor resistance as a function of the slip frequency.

With respect to the rotor leakage inductance, the saturation of the rotor bridges, if any, can be present and modelled as described in [28]. However, this effect can play a role only for very low load conditions where the rotor currents are small, and the bridges are not saturated. In these conditions, the computation of the IM efficiency is worthless as this tends to very low values regardless of the mechanical speed.

III. MEASUREMENT OF THE MODEL PARAMETERS

To perform an accurate efficiency mapping of the machine, it is necessary to know the IM parameters and their dependency on the previously reported nonlinearities. In this study, the IM parameters have been measured by executing the no-load and locked-rotor tests prescribed by well-established standards for sinusoidal supply [22], [23]. The tests have been conducted on the machine specified in Table I, using a programmable sinusoidal power supply source. With the need to identify a set of parameters accounting for the machine nonlinearities, it is straightforward to execute the above tests at different supply voltage and frequency values.

The stator resistance has been measured using the well-known volt-amperometric method, averaging three line-to-line values. The test temperature θ_0 must be recorded and considered as reference temperature for the measured resistance, allowing the correct computation of the Joule losses at different operating temperatures. The value of stator phase resistance $R_{s,0}$ measured on the tested IM is reported in Table II, together with the leakage inductances measured with the locked-rotor tests.

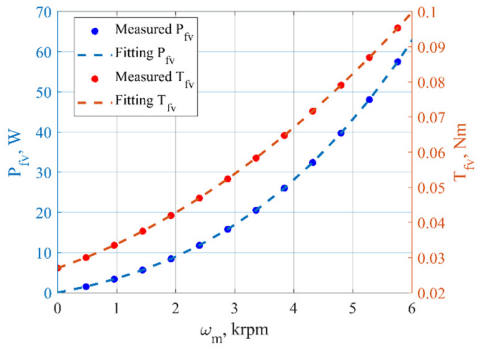

Fig. 3. Mechanical losses of the tested IM.

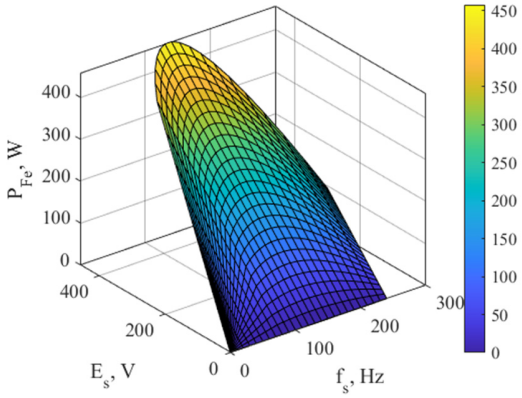

Fig. 4. Conventional iron losses map of the tested IM.

A. Locked-rotor test

The locked-rotor test is performed by imposing the machine rated current at different supply frequencies.

In order to determine the rotor resistance as a function of the slip frequency (to account for the skin effect on the rotor bar), the locked-rotor tests have been performed limiting the supply frequency in the range 5-40 Hz. The maximum test frequency has been limited to 40 Hz according to the operative values of the tested IM; in fact, for the case study the maximum slip frequency of the pull-out torque is never higher than 15 Hz. In this way, the skin effect on the stator resistance is practically always negligible and the rotor resistance can be estimated by the difference of the locked-rotor resistance and $R_{s,0}$ reported at the test temperature. The measured rotor resistance as a function of the slip frequency is reported in Fig. 2. By extrapolating at null frequency, the trend shown in this figure, the *dc* value of the rotor resistance is obtained.

The total leakage inductance L_{cc} has been measured at different supply frequencies in the range 40 – 200 Hz averaging the results.

The steady-state torque-speed rated characteristic (evaluated using the $R_{s,0}$, R_r, L_{cc} parameters) shows that IM under test is a NEMA Class A machine. Therefore, according to the regulatory standard [22], the ratio between stator and rotor leakage inductances is equal to one. Consequently, (9) can be used. Table II reports the measured values of overall-, stator-, and rotor- leakage inductance for the tested IM.

$$NEMA\ Class\ A \ \rightarrow\ L_{ls}/L_{lr} = 1 \ \Rightarrow\ L_{ls} = L_{lr} = L_{cc}/2 \quad (9)$$

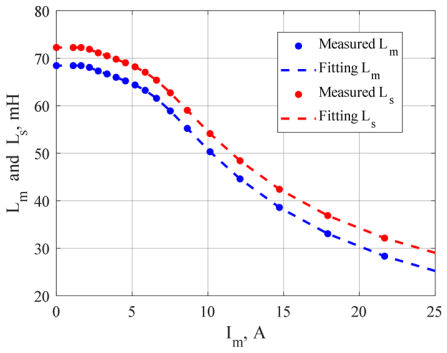

Fig. 5. Total stator inductance and magnetizing inductance of the tested IM.

B. *No-load test*

The no-load tests performed at different supply voltages and frequency values allow identifying the following quantities.

1) The friction and ventilation losses, usually referred to as mechanical losses, as a function of the rotational speed – shown in Fig. 3. According to the regulatory standard [22], the profile of no-load losses minus the I^2R expressed as a function of the supply voltage is considered. Thus, the mechanical losses P_{fv} are computed by extrapolating the intercept of this profile for a supply voltage equal to zero. Finally, the ratio between the mechanical losses P_{fv} and the mechanical speed ω_m, that is practically equal to the synchronous one, provides the value of the torque loss T_{fv}.
2) The iron losses P_{Fe}: these losses are the sum of the iron losses in the laminations, the rotor Joule losses induced by the harmonic contents of the air gap magnetomotive force (mmf) waveform and the skin effect contribution in the stator winding. It is worth mentioning that for traction motors equipped with hairpin windings, this contribution cannot a priori be neglected. In other words, the iron losses are the no-load losses minus the I^2R and the mechanical losses. The measured loss map for the tested IM is shown in Fig. 4 as a function of the supply frequency f_s and the back-emf E_s.
3) The total stator inductance L_s as a function of the magnetizing current I_m. Figure 5 shows the measured profiles of stator inductance and related magnetizing inductance L_m using (8) for the tested IM, both evaluated considering the 20 Hz no-load test results.

At this frequency, the mechanical losses and the skin effects are negligible, and the magnetizing current can be considered equal to the no-load current. In addition, there are no supply voltage limitations, and the test can be executed up to magnetizing currents comparable with the machine rated current.

IV. Inputs of Efficiency Mapping Procedure

The proposed efficiency mapping procedure requires the following input data and preliminary computations in order to estimate the IM efficiency map in the operative torque-speed range.

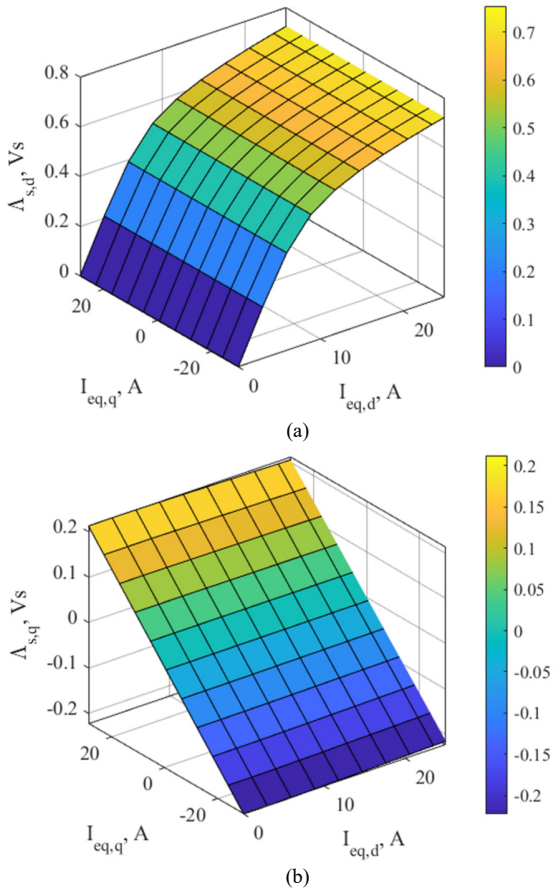

Fig. 6. Stator flux linkage *dq* maps of the tested IM.

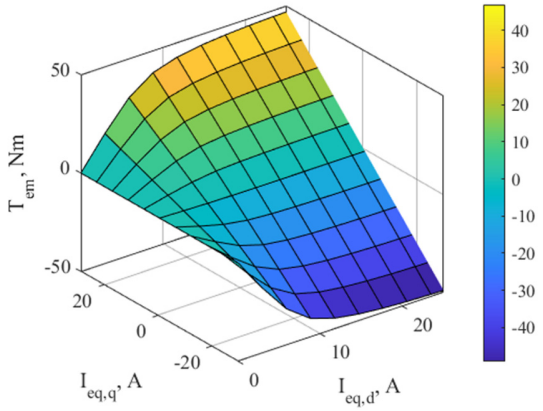

Fig. 7. Electromagnetic torque map of the tested IM.

A. *Input data*

1) Amplitude limit of the phase currents I_{max}: it usually consists of the minimum value between the overload motor current and the current limit of the inverter.
2) Limit of the phase voltage V_{max}: this value is the maximum amplitude of the fundamental voltage component provided by the PWM inverter. For the case study, a space vector modulation has been considered. Thus, (10) can be used, where v_{dc} is the input dc voltage of the inverter [26].

$$V_{max} = v_{dc} / \sqrt{3} \tag{10}$$

3) The stator and rotor operating temperatures θ_s, θ_r: the stator temperature is chosen according to the thermal limits of the machine or directly by the temperature load tests if available. In absence of further specific information, it is advisable to assume the rotor temperature equal to the stator one.
4) The machine parameters extracted by elaborating the no-load and locked-rotor tests, including the friction and windage loss trend – see Section III.
5) Flux and torque maps of the tested IM – these maps correlate the flux- and torque- producing (dq) currents ($I_{eq,d}$,I_{eq},q) with the steady-state values of (dq) stator flux linkages ($\Lambda_{s,d}$,$\Lambda_{s,q}$) and electromagnetic torque T_{em}.

B. Computation of flux and torque maps

Flux- and torque- maps of the tested IM are computed from the results of the no-load and locked-rotor tests using the procedure reported in the following.

1) Determination of the magnetizing current I_m: it can be expressed in terms of the flux- and torque- producing currents ($I_{eq,d}$, $I_{eq,q}$), as shown in (11).

$$I_m = \sqrt{{I_{eq,d}}^2 + {I_{eq,q}}^2 \cdot \left(1 - \frac{L_m}{L_m + L_{lr}}\right)^2} \tag{11}$$

Since the magnetizing inductance L_m is higher than the rotor leakage one L_{lr}, regardless of the saturation condition it is reasonable to assume that $I_m \cong I_{eq,d}$.

2) Definition of the ($I_{eq,d}$, $I_{eq,q}$) grid: a regular and coarse mesh grid of flux- and torque-producing dq currents is defined in (12), where $I_{m,max}$ is the maximum value of magnetizing current used in the no-load tests.

$$\begin{aligned} 0 \le I_{eq,d} \le I_{m,max} \\ -I_{max} \le I_{eq,q} \le I_{max} \end{aligned} \tag{12}$$

3) Computation of the flux-maps on the selected ($I_{eq,d}$, $I_{eq,q}$) grid: the dq stator flux linkages in steady-state conditions ($\Lambda_{s,d}$, $\Lambda_{s,q}$) are computed using (2) for each point of the mesh grid. An example of the computed flux maps for the tested IM are shown in Fig. 6(a) and Fig. 6(b).
4) Computation of the torque map on the selected ($I_{eq,d}$, $I_{eq,q}$) grid: when the above stator flux maps are known, it is straightforward to compute the electromagnetic torque (4). Figure 7 shows the obtained map for the considered IM. It is noted that the torque map includes both motor and generator operations due to the assumed symmetrical limits for the q-axis current.

V. Efficiency Mapping Procedure

The efficiency map is defined on the torque-speed domain. For this reason, a dense $\Delta\omega_m$ and ΔT_m discretization is assumed to generate a regular mesh grid. The speed limit of the grid is selected equal to the maximum operative speed of the machine, while the absolute torque limit corresponds to that of the torque map previously computed in the plane ($I_{eq,d}$, $I_{eq,q}$). Therefore, the efficiency map is obtained computing the efficiency in all the torque-speed points of the grid, even if some points can overcome the maximum torque per speed (MTPS) profile [29]. However, the proposed efficiency mapping procedure automatically rules out these points applying the voltage and current limits. The flowchart in Fig. 8 shows the step-by-step algorithm to compute the efficiency in any point of the defined torque-speed grid. In the figure, the numbering refers to the steps hereafter briefly described.

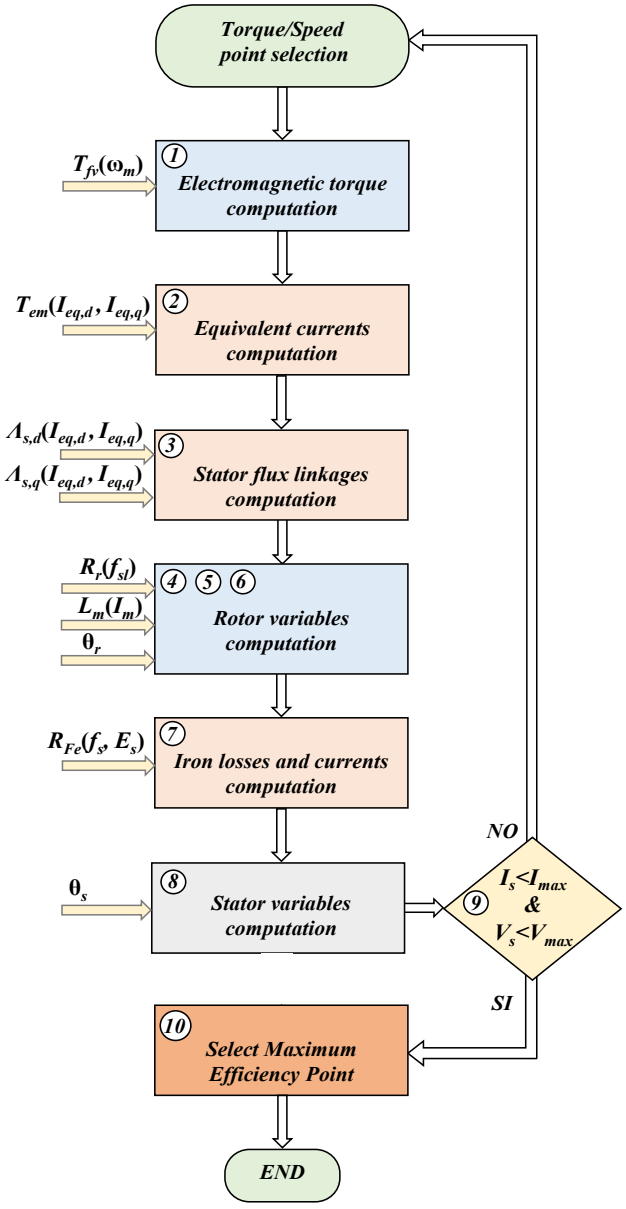

Fig. 8. Flow diagram of the efficiency computation for a defined (T_m, ω_m) combination.

Step 1: electromagnetic torque

The electromagnetic torque T_{em} is computed summing the considered shaft torque T_m and the friction and ventilation torque T_{fv} evaluated at the considered speed – Fig. 3.

Step 2: torque-producing equivalent currents

The electromagnetic torque computed at the Step 1 reflects in an isocontour on the surface shown in Fig. 7. This means that there are infinite ($I_{eq,d}$, $I_{eq,q}$) combinations that generate the

imposed torque [30], [31]. The isocontour is discretized in n_c points and the corresponding ($I_{eq,d}$, $I_{eq,q}$) values are stored in two n_c-dimensional vectors denoted as $I_{eq,d}^{vct}$ and $I_{eq,q}^{vct}$ (superscript '*vct*' stands for vector variables). The number n_c is variable with the electromagnetic torque value and with the discretization assumed for the torque.

Step 3: stator flux linkages

For each combination of the equivalent *dq* currents, the *dq* stator flux linkages are extracted by interpolating the flux maps shown in Fig. 6, obtaining the two n_c-dimensional stator flux linkage vectors $\Lambda_{s,d}^{vct}$ and $\Lambda_{s,q}^{vct}$.

Step 4 & Step 5: computation of the machine inductances and rotor current and flux

For each combination of the equivalent *dq* currents, it is possible to estimate the magnetizing inductance (under the assumption $I_m \cong I_{eq,d}$) obtaining the n_c-dimensional vector of magnetizing inductance L_m^{vct}. Finally, the vectors of total stator and rotor inductances (L_s^{vct} and L_r^{vct}) are computed using (8).

Using (3), the n_c-dimensional vectors of *q*-axis rotor current $I_{r,q}^{vct}$ and rotor flux linkage Λ_r^{vct} are computed.

Step 6: slip speed, rotor resistance and rotor Joule losses

The slip speed ω_{sl} is computed by (5), thus noting how the rotor resistance R_r is required. However, the rotor resistance itself depends on the slip frequency f_{sl}, according to the experimental profile obtained from the locked-rotor tests – see Fig. 2. Then, the following implicit equation system is solved:

$$\begin{cases} \omega_{sl}^{vct} = 2\pi \cdot f_{sl}^{vct} = \dfrac{R_r^{vct}}{L_r^{vct}} \cdot \dfrac{I_{eq,q}^{vct}}{I_{eq,d}^{vct}} \\ R_r^{vct} = R_{r,0}^{vct}\left(f_{sl}^{vct}\right) \cdot K_\theta^r \end{cases} \quad (13)$$

where $R_{r,0}^{vct}(\omega_{sl}^{vct})$ stands for the experimental dependency of the rotor resistance to the slip frequency shown in Fig. 2. In contrast, the coefficient K_θ^r considers the variation of the rotor resistance to the operating rotor temperature θ_r as $K_\theta^r = (k_r + \theta_r)/(k_r + \theta_0)$, where k_r is equal to 234.5 °C and 225 °C for the copper and aluminum, respectively. Finally, the n_c-dimensional vector of rotor Joule losses $P_{j,r}^{vct}$ is computed as:

$$P_{j,r}^{vct} = (3/2) \cdot R_r^{vct} .* I_{r,q}^{vct} .* I_{r,q}^{vct} \quad (14)$$

Step 7: computation of iron losses and iron currents

From the slip speed ω_{sl}^{vct}, the corresponding vector of synchronous speed ω_s^{vct} is computed by (5). At the same time, the n_c-dimensional vector of the stator frequency f_s^{vct} is easily obtained as $f_s^{vct} = \omega_s^{vct}/2\pi$. Therefore, the *dq* components ($E_{s,d}^{vct}$, $E_{s,q}^{vct}$) and amplitude E_s^{vct} of the machine's back-emf are computed by (1).

The iron losses, including the stator skin effect, are evaluated from the stator frequency and amplitude of the machine's back-emf by interpolating Fig. 4. Therefore, the n_c-dimensional vector of iron losses P_{Fe}^{vct} is obtained, while the corresponding current components ($I_{Fe,d}^{vct}$, $I_{Fe,q}^{vct}$) are computed using the IM equivalent circuit shown in Fig. 1.

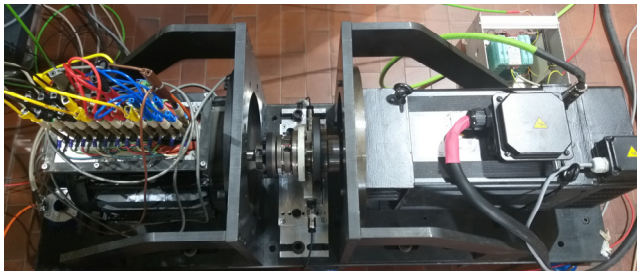

Fig. 9. View of the IM under test (left), torque transducer (center), and driving machine (right).

Step 8: stator currents, voltages and Joule losses

According to the IM equivalent circuit shown in Fig. 1, the n_c-dimensional vectors of *dq* stator currents ($I_{s,d}^{vct}$, $I_{s,q}^{vct}$) are computed, as well as the *dq* stator voltages ($V_{s,d}^{vct}$, $V_{s,q}^{vct}$). For this calculation, it is important referring the stator resistance R_s to the considered operative temperature of the stator winding. Finally, the n_c-dimensional vector of the stator Joule losses $P_{j,s}^{vct}$ can be computed.

Step 9 & Step 10: application of the voltage and current limits and selection of the maximum efficiency point

At these steps, the amplitude of the stator phase voltages V_s^{vct} and stator phase currents I_s^{vct} can be easily computed knowing their (*dq*) components. Therefore, all the elements of the n_c-dimensional vectors computed in the previous steps that do not respect the I_{max} and/or V_{max} limits are ruled out. Obviously, for the grid points that overcome the MTPS profile, and therefore cannot be physically operated, the algorithm skip the computation of the efficiency moving to consider the next torque-speed combination, as shown in Fig. 8.

At the end, the n_c-dimensional vector of the efficiencies that respect the imposed limits is obtained. In this vector, it is possible to determine the cell index for the maximum efficiency for the assumed (T_m,ω_m) point using (15). This index, denoted with superscript '*opt*', allows the extraction of the variable of interest in the maximum efficiency condition.

$$X^{opt} = \min\left(P_{j,r}^{vct}\Big|_{\substack{V_s^{vct} \le V_{max} \\ I_s^{vct} \le I_{max}}} + P_{Fe}^{vct}\Big|_{\substack{V_s^{vct} \le V_{max} \\ I_s^{vct} \le I_{max}}} + P_{j,s}^{vct}\Big|_{\substack{V_s^{vct} \le V_{max} \\ I_s^{vct} \le I_{max}}} \right) \quad (15)$$

In detail, the combination ($I_{s,d}^{opt}$, $I_{s,q}^{opt}$) leading to maximizing the efficiency is stored as reference (*dq*) currents to be imposed in the tested IM for the experimental validation that will be presented in Section VI.

Repeating the discussed algorithm for the whole torque-speed region, the proposed procedure can map not only the efficiency, but all the electromagnetic variables, thus representing a solution for accurately virtualize IMs operated in wide torque-speed ranges.

VI. Experimental Validation

The proposed efficiency mapping procedure has been validated comparing the computed and the measured efficiency maps for the 10 kW, 4-pole IM presented in [32]. For the purposes of this research activity, the stator windings of the considered IM prototype have been connected in three-phase

configurations. Both positive and negative torque values have been considered in the measurement procedure to validate the proposed efficiency mapping approach both for motor and generator operation modes.

A. Test rig

The machine under test has been mounted on a test rig and connected to a driving machine that acts as a speed-controlled prime mover, as shown in Fig. 9.

The IM under test has been supplied with a three-phase inverter with IGBT power modules rated 50A and 1200V, fed by a bidirectional programmable *dc* source. The switching frequency has been set at 8 kHz, with a software-implemented dead-time of 3 μs. The digital controller consists of the fast-prototyping board dSPACE MicroLabBox with the sampling frequency set at 8 kHz, single-edge PWM.

B. Efficiency maps measurement

The torque, speed and position have been measured using the transducer HBM T40B, mounted along with the mechanical coupling between the IM under test and the driving machine (see Fig. 9).

Concerning the electric measurements, the IM's phase currents have been measured using the high-performance current transducers LEM IT 200-S Ultrastab. The line-to-line PWM voltages have been measured using the HBM GN610B, consisting of a voltage card equipped with high-voltage/high-speed acquisition channels (1000 V, 18 bit, 2 MS/s).

Both mechanical and electrical quantities have been sampled and stored with a sampling frequency of 2 MS/s using the data recorder HBM GEN2tB [33]. In this way, using the data elaboration software integrated with the instrument, the time-fundamental electric power of the IM has been computed.

In summary, the experimental efficiency maps have been computed considering several fundamental electric periods for each test point. In this time window, the average values of mechanical power and fundamental electric power have been calculated, allowing the evaluation of the IM's efficiency considering its fundamental behaviour, i.e., the same one calculated by the proposed efficiency mapping procedure.

C. Test conditions

The experimental efficiency maps have been obtained controlling the IM with a user-implemented field-oriented control scheme that estimates the position of the *d*-axis with a calibrated flux observer. For each measurement point in the torque-speed plane, the implemented current vector control imposes the *dq* current components predicted by the previously presented efficiency mapping algorithm.

All efficiency maps have been evaluated at the same operating temperature in which the no-load and locked-rotor tests have been performed, (i.e., $\theta_0 = 25°$ C). The IM under test is equipped with only one temperature sensor (thermistor NTC) placed on the stator winding. Also, even loading the IM at the rated torque and waiting for the steady-state thermal conditions, the temperature of the rotor.

To guarantee that the tested IM practically operated in steady-state thermal conditions over the whole efficiency mapping procedure (i.e. $\theta_0 = 25°$ C), an adequate pause time has waited between one test point and the next. In detail, for the case study, it has been experimentally verified that 3 s on and 60 s off was sufficient to keep reasonably constant the stator winding temperature.

D. Measured and computed efficiency maps comparison

Figure 10 and Fig. 11 report the computed and the measured efficiency maps obtained for the *dc*-link voltages of 400 V and 600 V, respectively. The current limit for the mapping procedure has been set equal to the maximum machine overload current, that is equal to 25 A_{pk} for the tested IM. All the maps have been evaluated for several working points, with a resolution step of 2 Nm in torque and 400 rpm in speed. In Fig. 10 and Fig. 11 the considered working points are indicated by white dots, while the efficiencies below the above-mentioned resolution steps have not been represented.

Comparing the color shade maps in Fig. 10(a) and Fig. 11(a) for the computed efficiency with the corresponding measured maps shown in Fig. 10(b) and Fig. 11(b), respectively, it is well evident that the proposed mapping approach provides acceptable results for the complete torque-speed range. Also, comparing the results for the different *dc* voltage levels, both the computed and the experimental maps well match the base speed value that define extension of the flux-weakening region.

To better highlight the accuracy of the proposed efficiency mapping procedure, Fig. 10(c) and Fig. 11(c) show the percentage error maps between computed and measured efficiencies for the two *dc*-link voltages. The obtained percentage error is almost always below 2% in the explored torque-speed ranges. Higher errors have been observed for: i) working points close to the MTPS profile: 3 – 4 %, and ii) for low speed–high torque working points in generator mode: 5 - 6 %. Regarding the test points near to the MTPS profile, it is highlighted that they represent the most critical ones for the motor control algorithm. Indeed, in these operating points, the performance of the motor control algorithm in estimating the *d*-axis position strictly depends on that in reconstructing the machine's back-emf accurately [34], i.e., assessing the inverter nonlinearities and the resistive voltage drops with high accuracy. Therefore, in test points near the MTPS profile, the motor control algorithm has not precisely imposed the reference (*dq*) stator currents, justifying the error between computed efficiencies and measured ones. In any case, it is highlighted that the error in the test points near the MTPS profile only sometimes exceeds than 2 %, but it never overcomes 4 %.

Finally, percentage errors larger than 5% have been obtained for working points at very low speed and high braking torques in generator mode. In such operating conditions, the IM efficiency is near zero, hindering its accurate evaluation. It is noted how the experimental efficiency mapping of IMs is more challenging than the one performed for synchronous motors. Indeed, the *d*-axis position can be directly measured for these last, avoiding the implementation of dedicated flux observers whose performance affects the steady-state torque and efficiency [34].

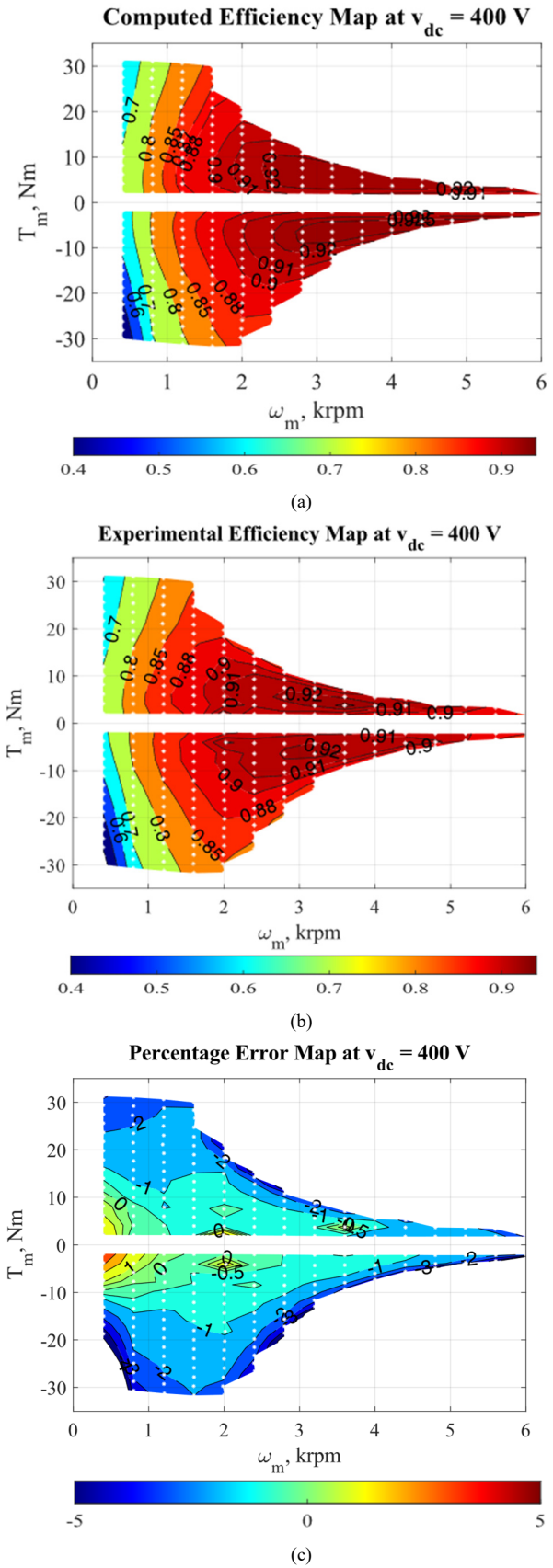

Fig. 10. Efficiency maps at v_{dc} = 400 V: a) computed, b) measured and c) related percentage error map computed as $100*(\eta_{comp} - \eta_{meas})/\eta_{meas}$.

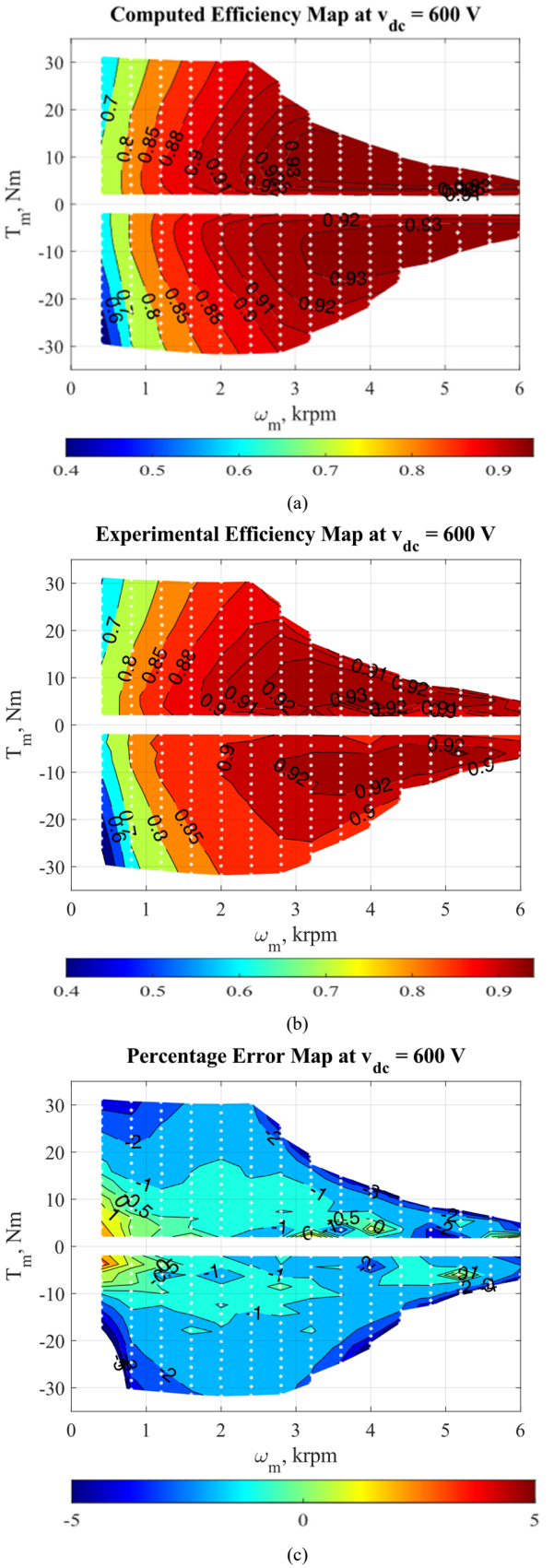

Fig. 11. Efficiency maps at v_{dc} = 600 V: a) computed, b) measured and c) related percentage error map computed as $100*(\eta_{comp} - \eta_{meas})/\eta_{meas}$.

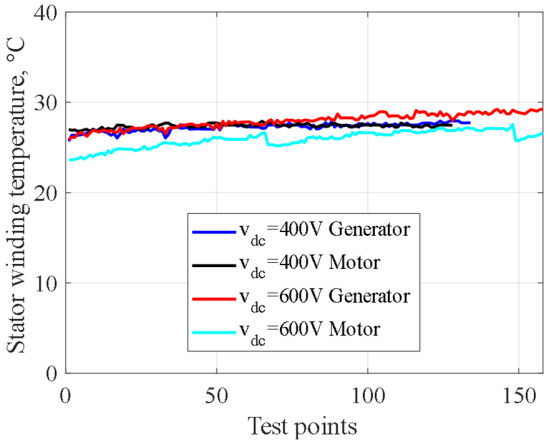

Fig. 12. The stator winding temperatures during the measured efficiency mapping.

Indeed, orientation errors introduced by the flux observer lead to imposing actual (*dq*) stator currents different from the reference ones, compromising the validation. In the author's opinion, this drawback is why very few contributions concerning the experimental efficiency mapping of IMs are reported in the literature.

Figure 12 demonstrates that the stator winding temperature measured with the embedded NTC sensor is reasonably constant during each mapping (i.e., around 3 – 4°C and θ_0 = 25° C). The first point of each curve corresponds to that at minimum speed and torque (i.e., 400 rpm, ± 2 Nm), while the last test point corresponds to that at maximum speed (6000 rpm) and maximum torque on the MTPS profile.

VII. Remarks

As previously reported, the proposed mapping algorithm computes efficiency maps with the aim to minimize the overall electrical losses (15). In other words, there is only one specific combination of (*dq*) variables (voltages, currents, fluxes) that leads to maximizing efficiency for the considered torque-speed point. However, the mapping algorithm can be modified to compute the efficiency maps to minimize the stator Joule losses, i.e., considering the machine's maximum torque per ampere (MTPA) operation for mechanical speeds lower than the base speed. In practice, focusing on the flowchart of Fig. 8, the block number 10 should change from "Select Maximum Efficiency Point" to "Select Minimum Stator Joule Losses". Conversely than (15), if the efficiency maps are computed to minimize the stator Joule losses, then the optimal element of the n_c-dimensional vectors X^{vct} is thus selected as:

$$X^{opt} = \min\left(P_{j,s}^{vct} \Big|_{\substack{V_s^{vct} \le V_{max} \\ I_s^{vct} \le I_{max}}} \right) \tag{16}$$

In Fig. 13, the efficiency map computed using the minimization of stator Joule losses at v_{dc} = 400 V is reported. Qualitatively, it is noted how the optimization strategy that maximizes the efficiency (see Fig. 10 (a)) leads to better results as the high efficient region is wider than the one obtained if only the stator Joule losses (Fig. 13) are minimized.

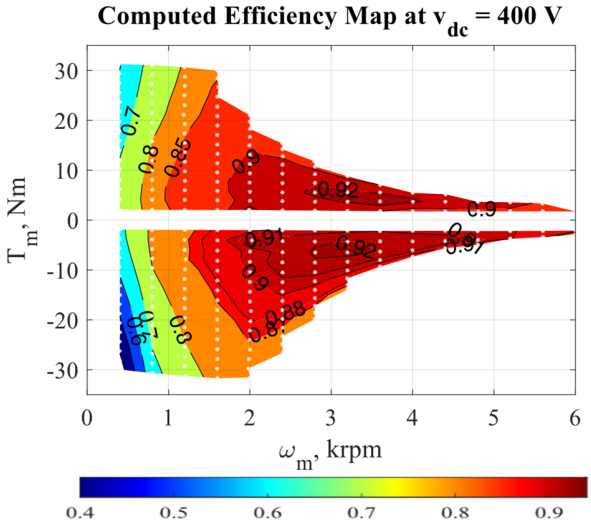

Fig. 13. Efficiency maps at v_{dc} = 400 V using the minimization of the stator Joule losses (MTPA).

About the maximum torque per voltage (MTPV) operation of the machine, this is automatically implemented. Indeed, for mechanical speeds higher than the base speed, the working points over the MTPV profile are automatically ruled out.

A further remark about the proposed efficiency mapping concerns the sinusoidal approach. In this paper, it has been chosen to focus only on the fundamental machine's efficiency since the impact of PWM significantly depends on the considered inverter, hindering the implementation of analytical losses models. Indeed, according to [35], the harmonic content introduced by the PWM modulation depends on the switching frequency, dc-link voltage level, inverter levels, modulation technique, amplitude- and frequency- modulation indexes (i.e., the amplitude and frequency of the fundamental phase voltages, respectively). Therefore, even computing the efficiency maps of the machine considering PWM modulation, this analysis cannot be generalized and must be performed again if the inverter or any of the above variables is changed. In addition, accurate analytic models of both iron and copper losses under PWM modulation are not reported in the literature, thus still representing an open research field. For these reasons, in this paper, it has been preferred to focus on an efficiency mapping algorithm for IM that considers only the time-fundamental behaviour, regardless of the inverter supplying the machine [36].

VIII. Conclusion

This paper proposed a methodology for computing the efficiency maps of induction machines operated in wide torque-speed ranges. In particular, the approach is based on the IM equivalent circuit whose parameters can be obtained by no-load and locked-rotor tests executed at different voltage and frequency values. Therefore, a set of efficiency maps are computed for different supply voltages and machine working temperatures, taking into account machine nonlinearities due to magnetic saturation, skin-effect, and iron losses.

The experimental validation for different *dc*-link voltages and the machine at ambient temperature has been conducted on

a 10 kW 4-pole IM prototype. The comparison between computed and measured efficiency maps shows a percentage error below 2% in most of the investigated torque-speed range, both for motoring and generator operation modes.

The main advantage of the proposed mapping approach relies on the possibility of obtaining efficiency maps for the induction machine, without the need for expensive test rigs or details on the machine design data. In this way, IMs can be easily virtualized to perform energetic assessments on the final application, even if motor prototypes are not still available.

ACKNOWLEDGMENT

The authors would like to acknowledge the support from the Power Electronics Innovation Center (PEIC) of Politecnico di Torino (www.peic.polito.it).

REFERENCES

[1] A. EL-Refaie, 'Toward a Sustainable More Electrified Future: The Role of Electrical Machines and Drives', *IEEE Electrification Mag.*, vol. 7, no. 1, pp. 49–59, Mar. 2019.

[2] S.S. Williamson, A. Emadi, and K. Rajashekara, 'Comprehensive Efficiency Modeling of Electric Traction Motor Drives for Hybrid Electric Vehicle Propulsion Applications', *IEEE Trans. Veh. Technol.*, vol. 56, no. 4, pp. 1561–1572, Jul. 2007.

[3] P.J. Ansell and K.S. Haran, 'Electrified Airplanes: A Path to Zero-Emission Air Travel', *IEEE Electrification Mag.*, vol. 8, no. 2, pp. 18–26, Jun. 2020.

[4] M. Bellone, M. Lundh, M. Wahde, and S. MacKinnon, 'Electrification and Automation in Maritime Applications: Employing AI Techniques for Energy Optimization and Efficiency', *IEEE Electrification Mag.*, vol. 7, no. 4, pp. 22–31, Dec. 2019.

[5] Q. Zhang, N. Cui, K. Li, Y. Shang and C. Zhang, 'Co-simulation of energy management strategy for hybrid electric vehicle in AVL InMotion', in 2017 Chinese Automation Congress (CAC), Oct. 2017, pp. 4932–4937.

[6] V. Groza, A. Merabet, C.D. Pitis, and V.D. Giurgiu, 'Novel method of pre-determining induction machine parameters and energetic efficiency', in 2013 IEEE Electrical Power Energy Conference, Aug. 2013, pp. 1–6.

[7] K. Li, S. Cui, A. Bouscayrol, and M. Hecquet, 'Analytical Derivation of Efficiency Map of an Induction Machine for Electric Vehicle Applications', in 2018 IEEE Vehicle Power and Propulsion Conference (VPPC), Aug. 2018, pp. 1–6.

[8] V.T. Buyukdegirmenci, A.M. Bazzi, and P.T. Krein, 'Evaluation of Induction and Permanent-Magnet Synchronous Machines Using Drive-Cycle Energy and Loss Minimization in Traction Applications', *IEEE Trans. Ind. Appl.*, vol. 50, no. 1, pp. 395–403, Jan. 2014.

[9] S. Williamson, M. Lukic, and A. Emadi, 'Comprehensive drive train efficiency analysis of hybrid electric and fuel cell vehicles based on motor-controller efficiency modeling', *IEEE Trans. Power Electron.*, vol. 21, no. 3, pp. 730–740, May 2006.

[10] W.Q. Chu *et al.*, 'Investigation on Operational Envelops and Efficiency Maps of Electrically Excited Machines for Electrical Vehicle Applications', *IEEE Trans. Magn.*, vol. 51, no. 4, pp. 1–10, Apr. 2015.

[11] A. Mahmoudi, W.L. Soong, G. Pellegrino, and E. Armando, 'Loss Function Modeling of Efficiency Maps of Electrical Machines', *IEEE Trans. Ind. Appl.*, vol. 53, no. 5, pp. 4221–4231, Sep. 2017.

[12] L. Song, Z. Li, Z. Cui, and G. Yang, 'Efficiency map calculation for surface-mounted permanent-magnet in-wheel motor based on design parameters and control strategy', in 2014 IEEE Conference and Expo Transportation Electrification Asia-Pacific (ITEC Asia-Pacific), Aug. 2014, pp. 1–6.

[13] M. Novak, J. Novak, Z. Novak, J. Chysky, ans O. Sivkov, 'Efficiency mapping of a 100 kW PMSM for traction applications', in 2017 IEEE 26th International Symposium on Industrial Electronics (ISIE), Jun. 2017, pp. 290–295.

[14] S. Stipetic, J. Goss, D. Zarko, and M. Popescu, 'Calculation of Efficiency Maps Using a Scalable Saturated Model of Synchronous Permanent Magnet Machines', *IEEE Trans. Ind. Appl.*, vol. 54, no. 5, pp. 4257–4267, Sep. 2018.

[15] S. Kahourzade, A. Mahmoudi, W.L. Soong, S. Ferrari, and G. Pellegrino, 'Correction of Finite-Element Calculated Efficiency Map using Experimental Measurements', in 2019 IEEE Energy Conversion Congress and Exposition (ECCE), Sep. 2019, pp. 5629–5636.

[16] L. Qi, F. Tao, W. Xuhui, T. Xiang, L. Ye, and Z. Guangzhen, 'Modeling of the efficiency MAP of surface permanent magnet machine for electrical vehicles', in 2013 International Conference on Electrical Machines and Systems (ICEMS), Oct. 2013, pp. 1222–1225.

[17] H. Sano, K. Narita, N. Schneider, K. Semba, K. Tani, T. Yamada, and R. Akaki, 'Loss Analysis of a Permanent Magnet Traction Motor in a Finite Element Analysis based Efficiency Map', in 2020 International Conference on Electrical Machines (ICEM), Aug. 2020, vol. 1, pp. 2301–2306.

[18] S. Ferrari, P. Ragazzo, G. Dilevrano, and G. Pellegrino, 'Flux-Map Based FEA Evaluation of Synchronous Machine Efficiency Maps', in 2021 IEEE Workshop on Electrical Machines Design, Control and Diagnosis (WEMDCD), Apr. 2021, pp. 76–81.

[19] F. Stanislav, B. Jan, and L. Jiri, 'Analytical derivation of induction machine efficiency map', in 4th International Conference on Power Engineering, Energy and Electrical Drives, May 2013, pp. 1206–1210.

[20] M. Carbonieri, N. Bianchi, and L. Alberti, 'Induction Motor Mapping Using Rotor Field-Oriented Analysis Technique', in 2019 IEEE Energy Conversion Congress and Exposition (ECCE), Sep. 2019, pp. 2321–2328.

[21] R. Bojoi, E. Armando, M. Pastorelli, and K. Lang, 'Efficiency and loss mapping of AC motors using advanced testing tools', in 2016 XXII International Conference on Electrical Machines (ICEM), Sep. 2016, pp. 1043–1049.

[22] Standard Test Procedure for Polyphase Induction Motors and Generators, IEEE Standard 112-2017.

[23] Int. Standard IEC 60034-2-1, "Rotating Electric Machines Part 2-1: Standard methods for determining losses and efficiency from tests", 2014.

[24] O. Stiscia, S. Rubino, S. Vaschetto, A. Cavagnino, and A. Tenconi, 'Off-Line Efficiency Mapping of Induction Motors Operated in Wide Torque-Speed Ranges', in 2020 IEEE Energy Conversion Congress and Exposition (ECCE), Oct. 2020, pp. 1075–1082.

[25] G. R. Slemon, 'Modelling of induction machines for electric drives', *IEEE Trans. Ind. Appl.*, vol. 25, no. 6, pp. 1126–1131, Nov. 1989.

[26] P. Krause, O. Wasynczuk, S.D. Sudhoff, and S. Pekarek, "Analysis of Electric Machinery and Drive Systems", *John Wiley & Sons, Ltd*, 2013.

[27] A. Boglietti, A. Cavagnino, and M. Lazzari, 'Computational Algorithms for Induction Motor Equivalent Circuit Parameter Determination—Part II: Skin Effect and Magnetizing Characteristics', *IEEE Trans. Ind. Electron.*, vol. 58, no. 9, pp. 3734–3740, Sep. 2011.

[28] J. Pyrhonen, J. Tapani, V. Hrabovcova, "Design of Rotating Electrical Machines", *John Wiley & Sons, Ltd*, 2008.

[29] S.H. Kim and S.-K. Sul, 'Maximum torque control of an induction machine in the field weakening region', *IEEE Trans. Ind. Appl.*, vol. 31, no. 4, pp. 787–794, Jul. 1995.

[30] W. Deprez *et al.*, 'Iso efficiency contours as a concept to characterize variable speed drive efficiency', in The XIX International Conference on Electrical Machines - ICEM 2010, Sep. 2010, pp. 1–6.

[31] D. Vanhooydonck *et. al.*, 'Calculating energy consumption of motor systems with varying load using iso efficiency contours', in The XIX International Conference on Electrical Machines - ICEM 2010, Sep. 2010, pp. 1–6.

[32] G. Rizzoli, G. Serra, P. Maggiore, and A. Tenconi, 'Optimized design of a multiphase induction machine for an open rotor aero-engine shaft-line-embedded starter/generator', in IECON 2013 - 39th Annual Conference of the IEEE Industrial Electronics Society, Nov. 2013, pp. 5203–5208.

[33] 'Genesis High Speed Tethered Mainframes', *HBM*, Apr. 09, 2021. https://www.hbm.com (accessed Sep. 23, 2021).

[34] P.L. Jansen and R.D. Lorenz, 'A physically insightful approach to the design and accuracy assessment of flux observers for field oriented induction machine drives', *IEEE Trans. Ind. Appl.*, vol. 30, no. 1, pp. 101–110, Jan. 1994.

[35] A. M. Hava, R. J. Kerkman and T. A. Lipo, "Simple analytical and graphical methods for carrier-based PWM-VSI drives," in *IEEE Trans. on Power Electronics*, vol. 14, no. 1, pp. 49-61, Jan. 1999, doi: 10.1109/63.737592.

[36] E. B. Agamloh, A. Cavagnino, and S. Vaschetto, "Standard efficiency determination of induction motors with a PWM inverter source," *IEEE Trans. Ind. Appl.*, vol. 55, no. 1, pp. 398-406, Jan./Feb. 2019.